A 3D particle-based simulation of heat and mass transfer behavior in the EAGLE ID1 in-pile test

Zhang, Ting
Department of Applied Quantum Physics and Nuclear Engineering, Kyushu University

Morita, Koji
Department of Applied Quantum Physics and Nuclear Engineering, Kyushu University

Liu, Xiaoxing
Department of Applied Quantum Physics and Nuclear Engineering, Kyushu University

Liu, Wei
Department of Applied Quantum Physics and Nuclear Engineering, Kyushu University

他

出版情報：Annals of Nuclear Energy. 179, pp.109389-, 2024. Elsevier
バージョン：
権利関係：

A 3D particle-based simulation of heat and mass transfer behavior in the EAGLE ID1 in-pile test

Ting Zhang[a]
E-mail: zhang.ting.639@s.kyushu-u.ac.jp

Koji Morita[a,*]
*Corresponding author. E-mail: morita@nucl.kyushu-u.ac.jp

Xiaoxing Liu[a]
E-mail: liuxx85@mail.sysu.edu.cn

Wei Liu[a]
E-mail: liuwei@nucl.kyushu-u.ac.jp

Kenji Kamiyama[b]
E-mail: kamiyama.kenji@jaea.go.jp

[a] Department of Applied Quantum Physics and Nuclear Engineering, Kyushu University, 744 Motooka, Nishi-ku, Fukuoka, 819-0395, JAPAN
[b] Fast Reactor Cycle System R&D Center, Japan Atomic Energy Agency, 4002 Narita-cho, Oarai, Ibaraki, 311-1393, JAPAN

Abstract

The ID1 test was the final target test of the EAGLE experimental framework program. It was used to verify that during a core disruptive accident, the molten fuel could be discharged via wall failure of an inner duct in FAIDUS, a design concept for the sodium-cooled fast reactor. The ID1 results revealed that the wall failure behavior owed to the large heat flow from the surrounding fuel/steel mixture. The present study numerically investigated the heat transfer mechanisms in the test using the finite volume particle method in the three-dimensional domain. The thermal hydraulic behaviors during wall failure were reproduced reasonably. The present three-dimensional simulation mitigated inherent defects of our previous two-dimensional calculation and clarified that the solid fuel and liquid steel close to the outer surface of the duct can expose the duct to high thermal loads, resulting in the wall failure.

Keyworks: Sodium-cooled fast reactor; Core disruptive accident; Particle-based simulation; Molten pool heat transfer.

1. Introduction

The large-scale molten pool in a sodium-cooled fast reactor (SFR) formed during a core disruptive accident (CDA) has received much attention because fuel compaction in the pool could lead to re-criticality and endanger the reactor vessel. In the case of the Japanese SFR, the design idea of FAIDUS (i.e., a fuel subassembly with an inner duct structure) has been especially presented to avoid this scenario via preventing the formation of the large molten pool. The molten mixture can flow into the inner duct through the breakage and discharge from the reactive core before mass aggregation in the core (Suzuki et al., 2014; Kamiyama et al., 2014(1)).

List of Abbreviations: CDA: Core disruptive accident; CFL: Courant-Friedrichs-Lewy condition; FAIDUS: Fuel subassembly with an inner duct structure; FVP: Finite volume particle; IGR: Impulse Graphite Reactor; JAEA: Japan Atomic Energy Agency; PMS model: Passively moving solid model; SFR: Sodium-cooled fast reactor.

Aimed at evaluating the usefulness of FAIDUS for early accident termination in SFRs during CDAs, the Japan Atomic Energy Agency (JAEA) carried out the EAGLE (Experimental Acquisition of Generalized Logic to Eliminate re-criticalities) project (Konishi et al., 2006; Konishi et al., 2007). The final target test of the project, named ID1, was an in-pile test conducted in a core-simulated vessel of the Impulse Graphite Reactor (IGR). It was performed to demonstrate that the inner duct of FAIDUS could evacuate a molten mixture through a wall breakage effectively. In this test, a stainless-steel duct was filled with sodium coolant and erected at the inner of a fuel subassembly. Without enough cooling during the experiment, the temperature of the fuel pins which released fission energy increased rapidly, and the fuel pellets and steel claddings would be melted down to form a molten pool. Under the high thermal load from the surrounding fuel/steel mixture, the wall of the inner duct failed. With large amount of moveable fuel swarming into the breakage and discharging outside through the relocation path, it was deduced that the design concept of FAIDUS was effective (Konishi et al., 2006). Furthermore, the experimental results revealed that the high heat flux (~10 MW/m^2) from the surrounding mixture to the duct was the key contributor to the wall failure. To further investigate the thermal-hydraulic mechanisms during the failure process, in this study, a 3D numerical simulation adopting the finite volume particle (FVP) method was applied for the analysis of the results of the EAGLE ID1 test.

Code for safety analysis of a fast reactor, SIMMER-III, has been used to simulate the EAGLE ID1 test in recent years, using fluid-dynamic calculations based on various Euler approaches (Toyooka et al., 2013; Toyooka et al., 2016). However, the limitations of the empirical models in the code have prevented the accurate representation of the local thermal condition and material distribution near the duct wall, including the local formation of a fuel crust. The fuel crust was re-solidified fuel that locally attached to the outer surface of the duct when liquid fuel accumulated near the low-temperature duct. However, in SIMMER-III calculations, the fuel crust was assumed to cover the entire duct surface and served as a thermal resistance layer, resulting in underestimation of the heat flux from the molten mixture to the duct.

In contrast with the SIMMER-III code, an enhanced FVP method based on a fully Lagrangian approach does not use the empirical models (e.g., engineering correlations), and can still simulate multi-component, multi-phase flows effectively (Zhang et al., 2007; Liu et al., 2018). Our previous two-dimensional (2D) simulation of the ID1 test using the FVP method revealed that fuel re-solidified and formed the crust locally on the duct wall, and the heat flux could be up to 10 MW/m^2 even under the limiting effect of the fuel crust (Zhang et al., 2021).

In this study, to eliminate the effect of dimensional defects on 2D simulation results and to obtain more reasonable and accurate understanding for the large thermal load in the ID1 test, a three-dimensional (3D) simulation was performed using the enhanced FVP method. Furthermore, mechanisms of the mass and thermal transfer during the duct wall failure were investigated by comparing the results of the ID1 test and 2D and 3D simulations.

2. Overview of the EAGLE ID1 test and 2D particle-based simulation

2.1 EAGLE ID1 test

The EAGLE ID1 test was conducted in the IGR core vessel, which was installed with an inner duct and fuel subassembly. The main test section used in the ID1 test is schematically shown in Fig. 1. The inner diameter of the duct was 40 mm and its wall thickness was 2 mm. The duct was made from stainless steel and erected at the center of the subassembly. Seventy-five fuel pins constructed from 8.0 kg of UO_2 fuel pellets and 2.5 kg of steel cladding were arranged annularly around the duct in three columns. Each fuel pin was 450 mm tall and contained

a specified percentage of depleted UO_2 pellets. During the experiment, the test portion was heated to 570–670 K by an electric heater. The control rods were then withdrawn, and the fission reaction started in the 17%-enriched UO_2 pellets except for the depleted pellets located at the lower end portion of the fuel pins. Figure 2 shows the average power provided by the IGR core (Toyooka et al., 2013). The moment at which the control rods were withdrawn was chosen as time zero. After the withdrawal of the control rods, the power climbed for approximately 3 s and then remained constant for approximately 1.5 s before decreasing. At the above power setting, the fuel pins melted to form a molten mixture pool and began transferring large thermal energy to the duct approximately 4.2 s after the withdrawal of the control rods. Suffered with the sustained heat load, the wall failure locally occurred at the middle axial height (~108 mm) in a period of 4.9–4.95 s (Konishi et al., 2006).

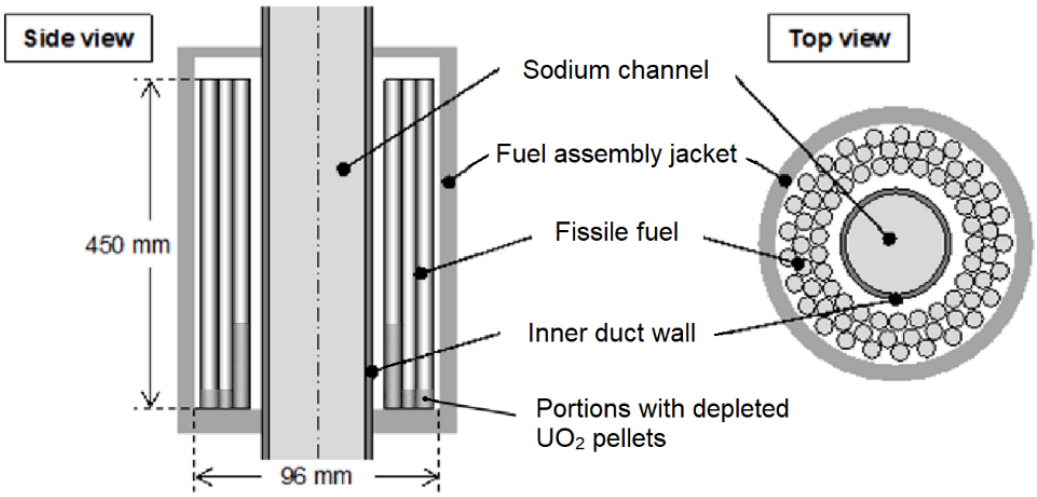

Fig. 1. Schematic of the main test section used in the EAGLE ID1 test.

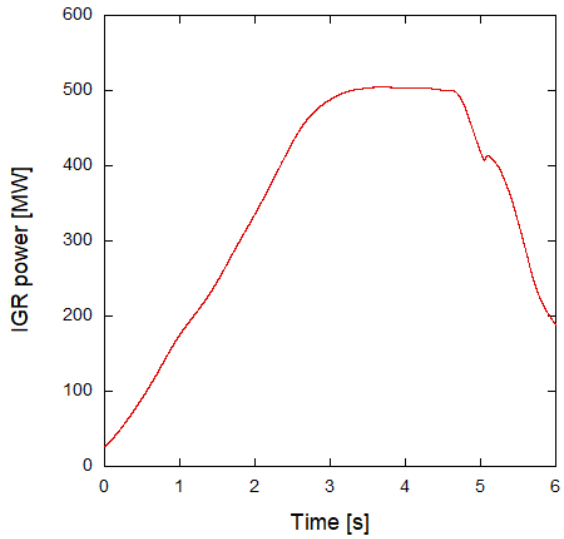

Fig. 2. Average IGR power in the EAGLE ID1 test.

2.2 2D particle-based simulation of the EAGLE ID1 test

In prior work, a 2D numerical simulation adopting the FVP method was performed to research the thermal-hydraulic behaviors, from disruption of the fuel pins to wall failure of the inner duct in the ID1 test (Zhang et al., 2021). To represent the mixing behavior of molten materials in the pool accurately, the temperature-dependence of the viscosity, which varied greatly with temperature, was considered for the liquid steel and fuel

in an improved 2D simulation of the ID1 test as follow-up work (Woodley et al., 1974; Kokubo et al., 2018). The main findings and conclusions of the follow-up 2D simulation, except for earlier heat transfer from pool to duct and wall failure of the duct due to good material mixing, were the same as those of the previous 2D simulation (Zhang et al., 2021). The following introduces the simulation conditions and results.

The ID1 test section is reproduced in an *x*–*z* Cartesian system. The simulation system with a height of 392 mm and width of 53 mm contained approximately 50,000 numerical particles, as shown in Fig. 3(a). The sizes of the fuel assembly region and fuel pins were set to realize an equivalent thermal load on the outer surface of the duct and ensure a same pool depth with the ID1 test. The width of the sodium was also matched the experimental conditions. The inserted power history of the fuel pins was consistent with the measured one during the test as shown in Fig.2. Additionally, the axial and lateral nuclear power profiles were considered on the basis of the experimental conditions.

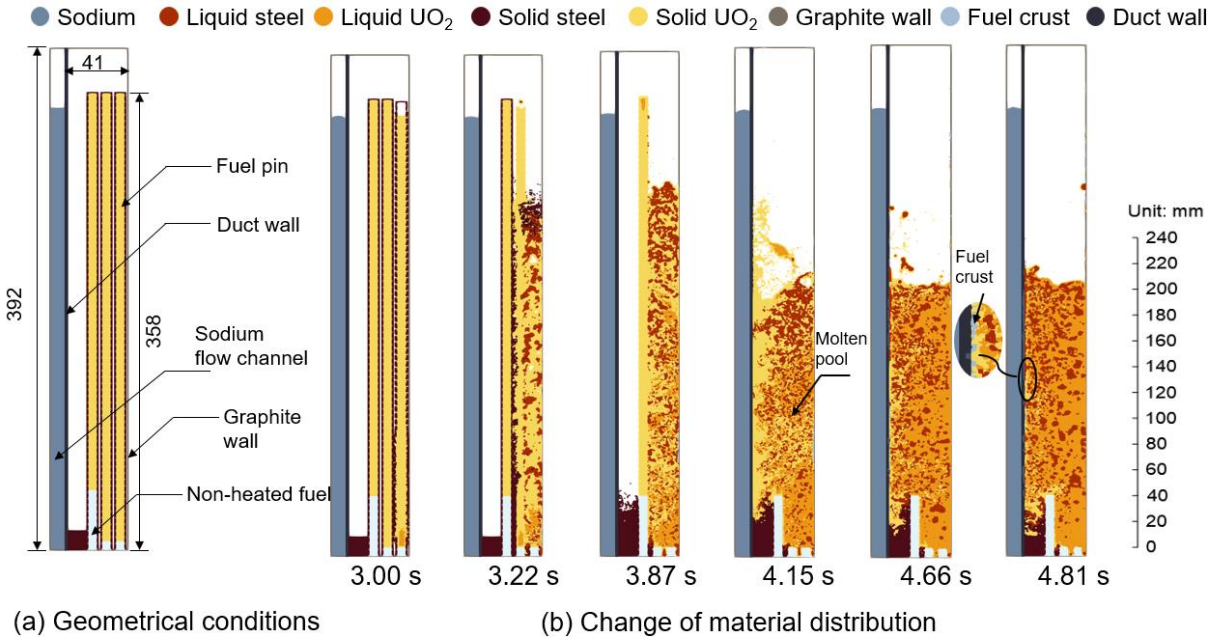

Fig. 3. Geometrical conditions and material distribution in the 2D simulation of the ID1 test.

Figure 3(b) shows the change of material distribution in the 2D simulation. The simulation results show that the outermost, middle and inner fuel pins began melting at 3.00, 3.22 and 3.87 s, respectively, after the withdrawal of the control rods. Being in contact with the high-temperature molten mixture, the duct wall at an axial height of approximately 108 mm was burdened with a high thermal load from 4.15 s, when the innermost fuel pin was disrupted completely. Meanwhile, a pool of a fuel/steel mixture formed. The high-temperature mixture contributed to the wall failure of the inner duct at 4.81 s.

A series of reasonable results was produced in the 2D simulation. However, without considering the disintegration and movement of fuel pellets, a large amount of liquid fuel with substantially higher thermal energy made contact with the outside surface of the duct, and the duct wall was melted through earlier than in the ID1 test. In turn, the sodium temperature at the upper-middle position near the inner surface of the duct increased to an abnormally high level. This will be discussed in detail in Chapter 5 by comparing the results with those of the 3D simulation.

3. Particle-based simulation method

As with the 2D simulation (Zhang et al., 2021), the 3D simulation for the EAGLE ID1 test was performed using the FVP method which was extended to the 3D calculation domain. Besides, the calculation for the radiation heat transfer was considered and a passively moving solid (PMS) model was used to solve the calculation for disruption and movement of fuel pins in the molten mixture.

3.1 Finite volume particle method

The full set of governing equations for incompressible multicomponent and multiphase flows are given as

$$\rho \frac{D\vec{u}}{Dt} = -\nabla p + \mu \nabla^2 \vec{u} + \vec{g} + \vec{f}, \tag{1}$$

$$\nabla \cdot \vec{u} = 0, \tag{2}$$

$$\rho \frac{DH}{Dt} = \nabla \cdot (k \nabla T) + Q. \tag{3}$$

Equation (1) is the Navier–Stokes equation where ρ is the density, $\vec{u}$ the velocity, t the time, p the pressure, μ the dynamic viscosity, $\vec{g}$ the gravitational force, and $\vec{f}$ represents the forces of surface tension and buoyancy per unit volume. For multicomponent and multiphase flows, the density and dynamic viscosity are smoothed near interfaces as introduced in our previous work (Zhang et al., 2008). It is a kind of arithmetic mean using the kernel function introduced by Monaghan (Monaghan, 2005). Equation (2) is the continuity equation. Equation (3) is from the energy equation, in which H the specific enthalpy, k the thermal conductivity, and T the temperature. The second term on the right-hand side of Eq. (3), Q, includes the nuclear heat, radiation heat per unit volume and the heat transfer rate at the interface between different phases. The nuclear power is arranged as described in Section 2.1.

The governing equations, including gradient and Laplacian terms, are discretized using the FVP approach. The FVP method represents the calculation domain with numerical particles, which carry material properties. Assuming that each particle occupies a certain volume, which is a circle in 2D calculation domain and a sphere in 3D domain, a particle interaction model could be derived. The velocity, position and temperature of the particles at each time step can be calculated from interactions with nearby particles covered with a kernel function. Based on particle-based method, the radiation heat transfer between two numerical particles *i* and *j* is calculated as

$$Q_{i,j} = \frac{\emptyset_{i,j}\sigma A\left\{\varepsilon_i\left(1-\varepsilon_j\right){T_j}^4 - \varepsilon_j(1-\varepsilon_i){T_i}^4\right\} + {\emptyset_{i,j}}^2\sigma A(1-\varepsilon_i)\left(1-\varepsilon_j\right)\left(\varepsilon_i{T_i}^4 - \varepsilon_j{T_j}^4\right)}{1-{\emptyset_{i,j}}^2(1-\varepsilon_i)\left(1-\varepsilon_j\right)}, \tag{4}$$

where σ is the Stefan–Boltzmann constant, A is the surface area of interaction between particles *i* and *j*, and ε_i and ε_j are respectively the emissivity of particles *i* and *j*, and $\emptyset_{i,j}$ is the radiation view factor between particles *i* and *j*. The surface area involved into the radiation between particles *i* and *j* is small enough, so that the radiation view factor is simply derived from its definition as

$$\emptyset_{i,j} = \frac{\cos\theta_i \cos\theta_j}{\pi\left|\vec{r}_{i,j}\right|^2} A. \tag{5}$$

In Equation (5), $\vec{r}_{i,j}$ is the vector of distance between particles *i* and *j*, θ_i and θ_j are the angles between the surface normal and a ray between particles *i* and *j*.

In the present simulation, we assume that multiple-reflection radiative heat transfer between particles can be neglected because of the small surface area that contributes to the radiation of each numerical particle used in the FVP method. In addition, the heat transfer between different phases is modeled as non-equilibrium and equilibrium transfer. Further details were reported in our previous paper on 2D simulation (Zhang et al., 2021).

3.2 PMS model

In addition to the melting behavior of fuel pellets, the existence of solid-phase materials such as solid-fuel pellets and re-solidified fuel in the molten pool and the interactions of these materials with the molten mixture will affect the convection of liquid-phase materials (Kamiyama et al., 2014(2)). Taking this effect into consideration, the PMS model is used in the 3D simulation. The PMS model, which was originally proposed to describe the motion of a solid lump in a fluid, is applied to simulate the disruption and displacement of fuel pins in the molten mixture (Koshizuka et al., 1998). In the first place, both liquid and solid particles are governed by Eqs. (1)–(3) based on the FVP method, according to which particles receive updated locations and velocities. The PMS model is then used to perform an extra procedure for solid particles exclusively. In the 3D simulation for the ID1 test, one fuel pellet is initially represented by a fixed number (i.e. 3950) of solid particles as a solid lump in the PMS modeling. After pin disruption, solid lumps that have been transferred to the fluid field can be made smaller by their own melting or larger by the solidification of melts onto solid lumps. It is noted that when the solid lumps impact the wall, they will be reflected to the inside of the pool. The translation velocity vectors and the center position of the lump are evaluated according to

$$\vec{U} = \frac{\sum_i m_i \vec{u}_i}{M}, \tag{6}$$

$$\vec{x} = \frac{\sum_i m_i \vec{x}_i}{M}. \tag{7}$$

The velocities of solid particles are replaced by calculating the rotation and translation motion of the lump (Koshizuka et al., 1998). Compared with 2D simulation, the 3D calculation coupled with the PMS model can simulate the disruption of fuel pins more reasonably and improve the simulation for the movement of solid lumps in the molten pool.

4. 3D simulation of the EAGLE ID1 test

4.1 Physical properties of materials

The physical parameters of the materials utilized in the simulation are listed in Table 1 (Fink et al., 1995; Fink, 2000; Fukuyama et al., 2019). It should be noted that the table shows parameter values of liquid UO_2 and stainless steel at their liquidus temperature, sodium at 700 K and solid UO_2 and stainless steel at 700 K. Meanwhile, the values of some parameters were constantly changing during the calculation as a result of changing temperature. For example, the temperature dependency of the viscosity of liquid phases was considered for the proper presentation of the mixing behavior of molten materials as in the follow-up 2D simulation. Additionally, the thermal conductivities of the materials changed largely with the temperature, and they were also concerned in the simulation. Constant values were used for material densities in the fluid-dynamic calculations, which assume incompressible fluids. The buoyancy caused by the density change with temperature was considered in the Navier-Stokes equation for fluid components. The surface tension between the liquid and solid phases, as well as the interfacial tension between liquids, was considered using an inter-particle potential force (Kondo et al., 2007).

Table 1. Physical parameters of materials applied in the simulation

	State	Viscosity [Pa·s]	Surface tension [N/m]	Thermal conductivity [W/(m·K)]	Density [kg/m^3]	Specific heat [J/(kg·K)]	Latent heat of fusion [J/kg]	Melting temperature [K]
UO_2	Liquid	4.34×10^{-3}	0.513	2.50	10,800	485	2.77×10^{4}	3,120 (liquidus) 3,120 (solidus)
	Solid	---	---	4.74		427		
Stainless steel	Liquid	10.98×10^{-3}	1.27	35.8	7,783	782	2.70×10^{4}	1,719 (liquidus) 1,666 (solidus)
	Solid	---	---	19.8		627		
Sodium	Liquid	2.56×10^{-4}	0.166	69.5	845	1,277	---	---

4.2 Modeling of the ID1 test conditions

In this simulation, the test section used in the ID1 test was recreated in a 3D domain, as shown in Fig. 4. The test section included a graphite wall, sodium flow channel, duct wall and fuel pins. From the top view, the cross section was in the shape of circular sector with a central angle of 14.4°. It reproduced part of the main test section shown in Fig.1 and contained three fuel pins. This geometrical condition not only made the simulation complexity less than that of the whole configuration simulation but also ensured the calculation accuracy to the greatest extent possible. The geometrical structure with a height of 510 mm and width of 55 mm was represented by 1,915,958 numerical particles. The fuel pins were constructed using solid fuel particles and solid stainless-steel particles to represent the fuel pellets and cladding, respectively. The size of fuel pins and the width of the fuel assembly region matched the ID1 test conditions. The width of the sodium flow channel was set at 10 mm, which was the hydraulic diameter of the inner duct in the test. The magnitude and profiles of inserted power applied to the fuel pins were in accordance with the power condition in the ID1 test.

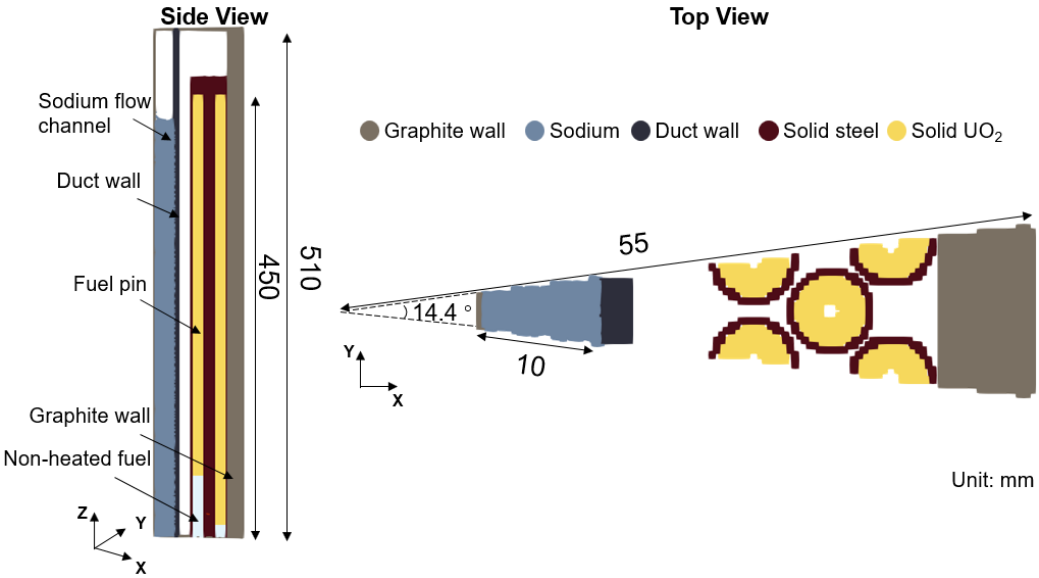

Fig. 4. Geometrical conditions in the 3D simulation of the EAGLE ID1 test.

The initial distance between numerical particles in this simulation was 0.4 mm. The initial time step size was 10^{-4} s. The Courant–Friedrichs–Lewy (CFL) condition was applied to adjust the time step size for computational stability and the Courant number was chosen as 0.2. In *x* and *z* directions enclosed by the graphite wall, the effect of thermal loss to the surroundings through the graphite wall was neglected and adiabatic boundary

conditions were assumed. For the *y* direction, because the calculation geometry was a small unit of the entire test configuration in the EAGLE ID1 test, the periodic boundary condition was realized by the interaction of particles on one of the periodic sides with particles on the other sides. To achieve high computational efficiency, a parallel calculation was performed on a supercomputer (Fujitsu PRIMERGY CX2550/CX2560 M4) with 36 × 128 cores. Under these conditions, it took approximately 100 hours to reproduce a 6-second simulation for one case.

4.3 Simulation results

4.3.1 Event behavior until failure of the duct wall

In the ID1 test, the outside, middle and inner fuel pins were disrupted successively, until a molten pool with high thermal energy formed. Under the large thermal load from the surrounding mixture from 4.2 s after the withdrawal of the control rods, the duct wall failed in the period of 4.9–4.95 s, when the thermocouple mounted on the inner surface of the duct first indicated an excessive temperature rise (Konishi et al., 2006). SIMMER-III simulation applied the calculation results of TAC2D, in which the duct wall failed when the local outer–surface temperature of the duct increased to 1625 K, for the deduction of duct wall failure initiation (Toyooka et al., 2013). In addition, in our 2D simulations, the wall failure of the duct was deemed to start when the temperature reached the liquidus temperature (1719 K) of stainless steel (Zhang et al., 2021).

The material distributions at several remarkable moments are shown in Fig. 5 to illustrate the event process in the 3D simulation. In Fig. 5, the side view (Fig. 5(a)) and transverse view at 190-mm height (Fig. 5(b)) are provided to show the relative position of fuel pins, formation of molten pool, and distribution of molten materials including solid lumps and fuel crust. At 3.19 and 3.61 s, when part of the steel cladding and a small quantity of fuel pellets melted into liquid, the outside and middle pins were disrupted as a number of solid lumps under the action of the PMS model successively. The solid lumps accumulated at the region of disrupted pins, with some of the molten mixture flowed through the gap between inner pins. At 4.10 s, the inner fuel pins were also disrupted.

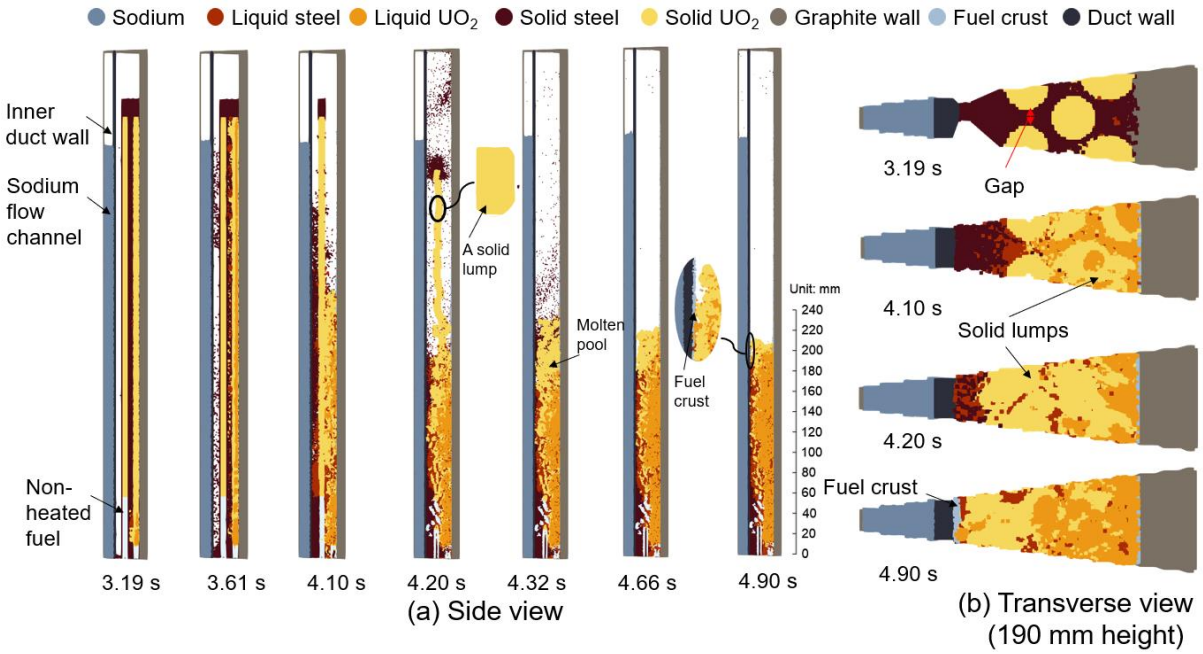

Fig. 5. Material distributions at various moments until failure of the duct wall.

In the analysis of the simulation, according to the test conditions, a temperature surge at an axial height of the

duct wall of 108 mm was chosen as the starting signal for overall pool-to-duct heat transfer. Figures 5 and 6 show that, with the disruption of the inner fuel pins, more and more molten mixture made contact with the outer surface of the duct and began imposing a thermal load on the duct at 4.20 s, which agrees well with the test results. At 4.32 s, the molten pool was fully formed with liquid fuel and steel and solid lumps.

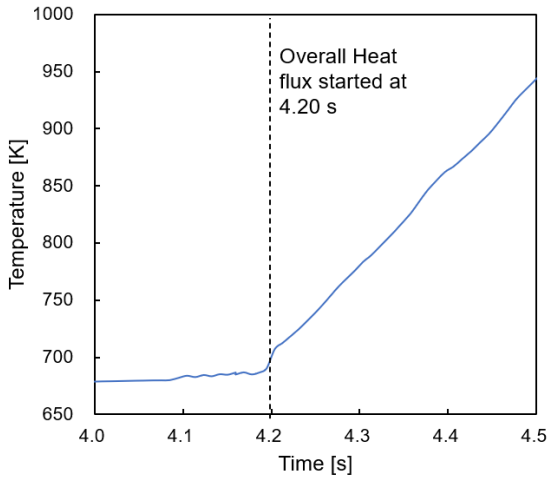

Fig. 6. Temperature of the duct wall at an axial height of 108 mm.

In the 3D simulation, considering the unclarified conditions of the duct wall when it was disrupted, we assume that the local wall might be melted through when the temperature of its outer surface was in the range of the solidus temperature (1666 K) to the liquidus temperature (1719 K) of stainless steel. Figure 7 shows that the local temperature of the duct increased more rapidly and firstly reached 1666 and 1719 K at the middle (90–110 mm) and upper axial region (180–200 mm), respectively.

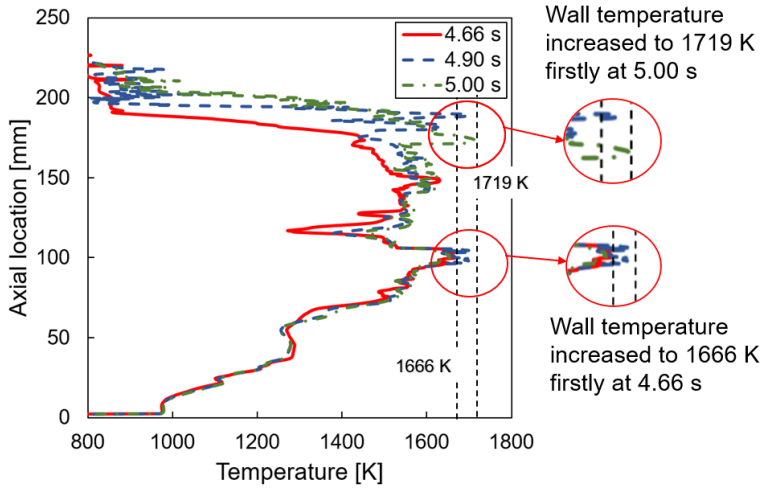

Fig. 7. Axial distributions of the outer-surface temperature of the duct at 4.66, 4.90 and 5.00 s.

The axial distributions of the sodium temperature near the inner surface of the duct at 4.66, 4.90 and 5.00 are shown in Fig. 8. For contrast, the sodium temperature measured at some specific positions in the ID1 test when the wall failure was detected are also illustrated in this figure. The figure shows that the sodium temperatures at 4.90 s were consistent with the ID1 results. According to the aforementioned studies on the wall temperature, despite the fact that the wall temperature remained lower than the liquidus temperature, the duct wall at the middle axial region (90–110 mm) was under a high thermal load for a longer time from 4.66 s and was firstly melted through after 4.90 s, compared with the wall at the upper position (180–200 mm). Likewise, in the ID1 test, it was at approximately this axial height that the thermocouple installed on the inner surface of the duct

first signaled contact with the high-temperature molten mixture (Konishi et al., 2006).

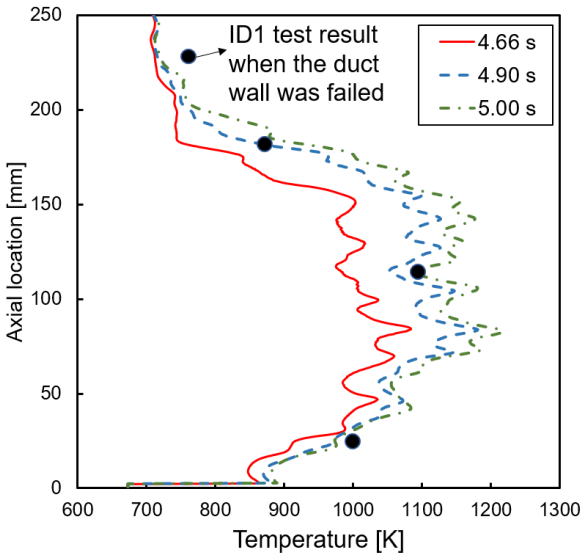

Fig. 8. Axial distributions of the sodium temperature at 4.66, 4.90 and 5.00 s.

4.3.2 Heat transfer behavior

In the ID1 test, the nuclear energy of the fuel was mainly used to melt the fuel pins for pool formation and heat the duct wall and sodium coolant for wall failure. Figure 9 depicts the change in the average temperature of the duct wall and the proportion of pool-to-duct transferred energy in the total transported energy of the pool system. The pool-to-duct transferred energy and pool-transported energy are the total amounts for 0.1-s intervals during the simulation. At 4.2 s, when the overall pool-to-duct heat flux started, approximately 12% of the transported energy was used to heat the duct wall and sodium coolant. The fraction decreased to 7% as the duct wall temperature increased. Until the duct wall failed, approximately 2% of the energy lost from the pool was in the form of thermal radiation in the present simulation.

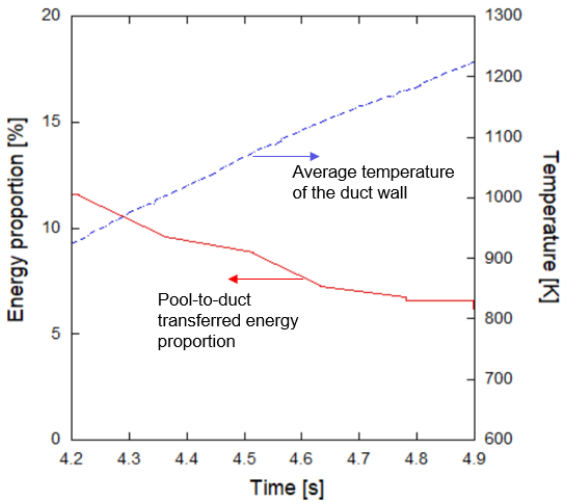

Fig. 9. Pool-to-duct transferred energy fraction in the total transported energy of the pool system and average temperature of the duct wall in the 3D simulation.

To demonstrate that the present 3D simulation improved the calculation for pool-to-duct heat flow and could reproduce more reasonable results of thermal-hydraulic behaviors than 2D simulations, we compared the axial

distributions of sodium temperature among test results and 2D and 3D simulation results. In the ID1 test when wall failure was detected, the measured temperature of the sodium was lower at the upper region near the molten pool surface and higher at the middle location where duct wall failure occurred. Figure 10 shows that, in comparison with an abnormal temperature peak of sodium in the upper-middle duct in the 2D simulation, the cause of which will be explained later in Chapter 5, the sodium temperature in the 3D simulation kept pace with the test results. This demonstrates that the calculation of heat transfer in the 3D simulation was more reasonable than that in the 2D simulation.

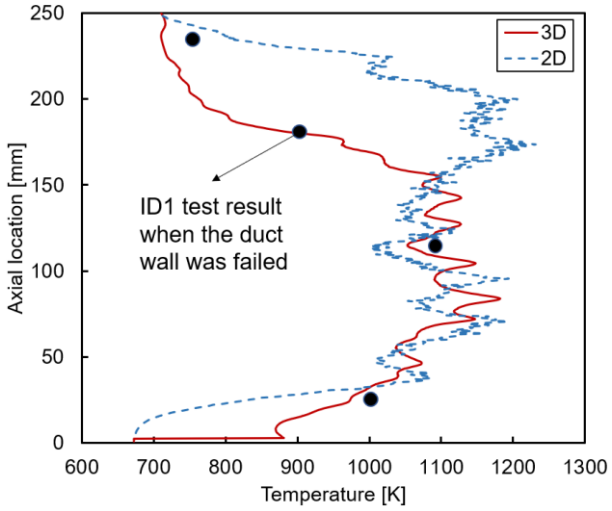

Fig. 10. Comparison of axial distributions of the sodium temperature near the inner surface of the duct among test results and 2D and 3D simulation results.

Figure 11 shows the axial distributions of pool-to-duct heat fluxes in the 3D simulation at 4.20, 4.66 and 4.90 s. It is seen that at 4.20 s, at the initiation of pool-to-duct heat transfer, the lower duct wall was exposed to a rather large heat flux (>10 MW/m^2). Fig. 5 shows that the lower wall contacted with a large amount of molten mixture at this moment. Followed by the formation of the molten pool, a higher heat flux was observed at a higher position of the pool. With time, the temperature difference between the inner and outer surface of the duct decreased, leading to a weaker heat flow from the lower pool. Meanwhile, the heat flux at the higher position (180–200 mm) increased continuously from 4.66 s. This will be explained in Subsection 4.3.3 on the effect of the material distribution.

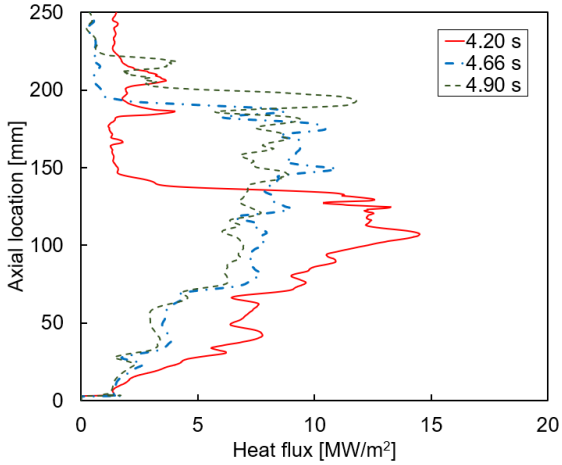

Fig. 11. Axial distributions of the heat fluxes from the molten pool to the inner duct at 4.20, 4.66 and 4.90 s.

4.3.3 Effect of the material distribution on failure of the duct wall

As mentioned above, the ID1 test results suggest that wall failure of the duct was caused by large thermal load from the surrounding molten mixture. We analyze here the effect of the material distribution on the duct-wall failure by studying the relationship between the heat flux and material distribution at the axial locations of 90–110 and 180–200 mm. We note that both axial locations are where the outer surface of the duct experienced high thermal pressure. Otherwise, according to the above analysis on sodium temperature, the duct wall might be melted through at the middle-height (90–110 mm) position firstly. In addition, the sodium temperature did not show an abnormal large magnitude at the higher (180–200 mm) position, like that in the 2D simulation as mentioned in Section 4.3.1.

Figure 12 shows the changes in pool-to-duct heat flux and outer-surface temperature of the duct at heights of 90–110 and 180–200 mm. Figure 13 presents the changes in crust thickness and volume fractions of the solid fuel, liquid fuel and steel close to the outer surface of the duct at heights of 90–110 and 180–200 mm. In this study, the materials existing within 4-mm radial distance from the outer surface of the duct were regarded to have a direct effect on the pool-to-duct heat flow. Figure 13 shows average values of the crust thickness and volume fractions of materials for the chosen axial region (20 mm) near the outer surface of the duct. It is seen after a weak heat flux from the molten pool, a continuous and large thermal flow was imposed on the local duct wall at a height of 90–110 mm from 4.10 s, causing a surge in the wall temperature. Considering the material distribution shown in Fig. 13(a), it is deduced that the early heat flux was due to liquid steel that flowed from the region of the disrupted fuel pins, while for a sustainable thermal source, the solid fuel was required to supply the heat energy. Making contact with the liquid steel having higher thermal conductivity (~35.8 W/(m·K)) and solid fuel having high temperature, the duct wall experienced a high thermal load. The increasing wall temperature in turn reduces the heat flux.

In a similar manner, we checked the history of material conditions at a height of 180–200 mm. Figures 12(b) and 13(b) show a similar effect of liquid steel and solid fuel on the heat flux at the upper position. Meanwhile, in contrast with the result for middle-height (90–110 mm) duct where little liquid fuel moved near its outer surface, a little liquid fuel accumulated near the higher wall surface. The increasing fraction of liquid fuel surrounding the higher duct wall offered enough thermal energy, and the heat flux from the molten pool to the duct wall kept rising. In the meantime, part of the liquid fuel would re-solidify and attach on the duct wall to form the solid fuel crust, restricting the transfer of heat from the molten mixture to the duct. As a result, even the outer-surface temperature of the duct reached the liquidus temperature, the duct wall would not be melted through immediately at the height of 180–200 mm, owing to its lower center and inner temperature at the thickness direction (<1400 K) and lower sodium temperature near the inner surface of the duct (<900 K).

Above all, contact between the outer surface of the duct and the liquid steel with high thermal conductivity and solid fuel with nuclear energy can transfer a substantial amount of thermal energy from the molten mixture to the duct, which in turn can lead to breakage of the wall. Furthermore, a little liquid fuel close to the outer-surface of the duct can enhance the pool-to-duct heat flux and meanwhile solidify to produce a fuel crust, limiting the heat flow from the molten pool and preventing the melting through of the inner duct.

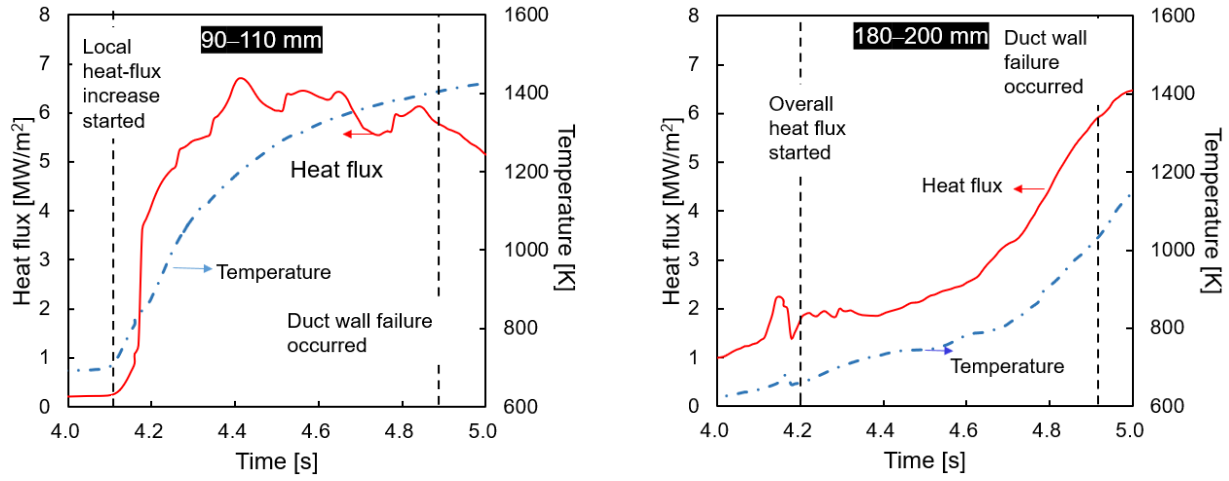

(a) 90–110 mm (b) 180–200 mm

Fig. 12. Heat fluxes (left axis) and temperatures (right axis) at axial locations of 90–110 and 180–200 mm.

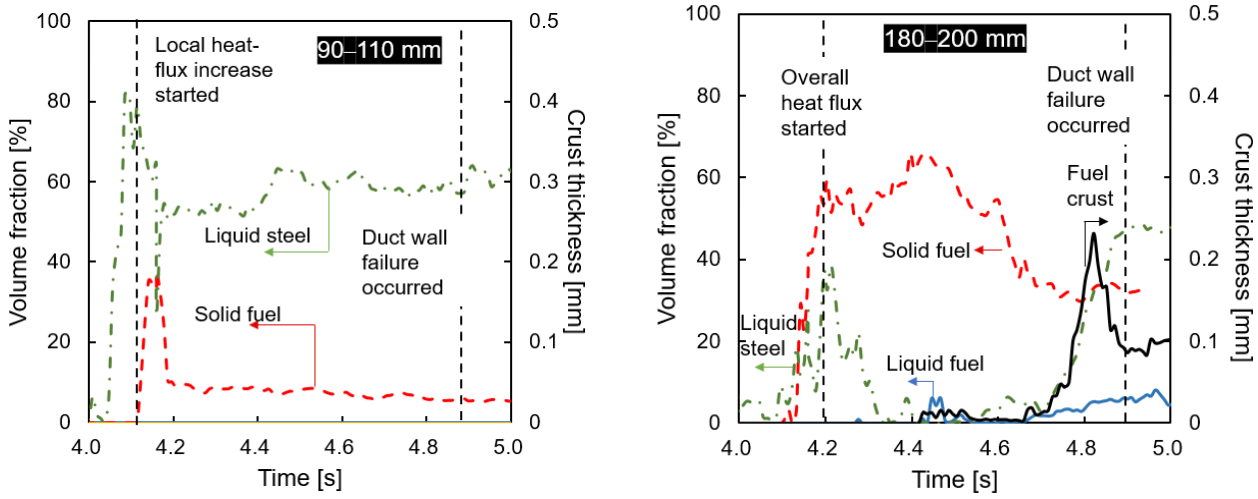

(a) 90–110 mm (b) 180–200 mm

Fig. 13. Volume fractions of the solid fuel, liquid fuel and steel (left axis) and crust thickness (right axis) at axial locations of 90–110 and 180–200 mm.

5. Discussion

The results of 3D simulation reported herein suggest that, early in the molten pool formation, liquid steel with good thermal conductivity transfers a little thermal energy to the duct wall, generating heat flux toward the duct as discussed in Section 4.3. With disruption of the inner fuel pins, solid fuel accumulates along the outer surface of the duct, increasing the pool-to-duct heat flux at local axial positions. In our follow-up 2D simulation of the EAGLE ID1 test, the fuel pins were disrupted when the fuel pellets melted into liquid and the duct was exposed directly to the molten fuel and steel. At this point, there was a transfer of heat from the molten mixture to the duct due to the molten fuel and steel making contact with the surface of the duct. We discuss here the differences in heat transfer mechanisms between the 2D and 3D simulations of the EAGLE ID1 test.

Figures 14 and 15 respectively show the axial distributions of the heat flux and the volume fractions of the fuel and liquid steel close to the outer surface of the duct at the moment of deduced wall failure of the duct in 2D and 3D simulations. In the two figures, the volume fractions were addressed by the simple moving average

method with a 10-mm step at the axial direction. The 2D simulation assumed that the molten mixture formed after the melting of the fuel pins. After the formation of the molten pool, the fuel in the pool remained in the liquid phase with only a little re-solidifying. Thus, as Fig. 14 shows, the thermal energy causing wall failure of the duct was mainly provided by liquid fuel in the 2D simulation. Under the much larger thermal impact of the liquid fuel, the duct wall was melted through earlier (at 4.81 s) than in the test.

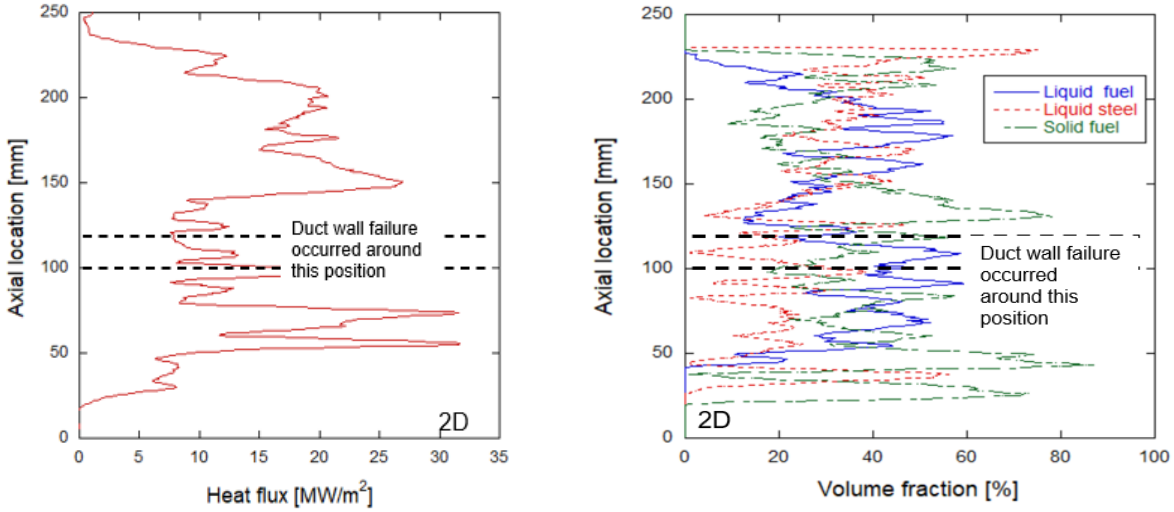

(a) Heat flux (b) Volume fractions of fuel and steel

Fig. 14. Axial distributions of the heat flux and volume fractions of the fuel and steel close to the outer surface of the duct at the moment of deduced wall failure of the duct in 2D simulation.

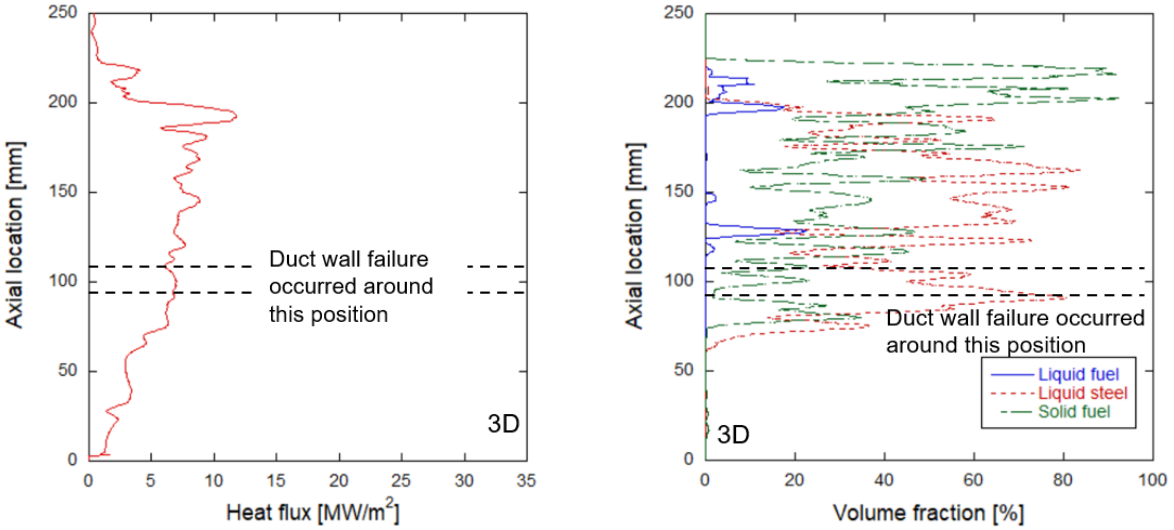

(a) Heat flux (b) Volume fractions of fuel and steel

Fig. 15. Axial distributions of the heat flux and volume fractions of the fuel and steel close to the outer surface of the duct at the moment of deduced wall failure of the duct in 3D simulation.

As mentioned in Section 3.2, the PMS model was applied in the 3D simulation to simulate the movement of solid materials in the pool. In PMS modeling, before melting into liquid, the fuel pins break into a number of solid lumps as shown in Fig. 5. Figure15 shows that most fuel approaching the outer surface of the duct was in a solid phase at the failure of the duct wall. Although the temperature of the solid fuel was lower than that of the liquid phase, a greater quantity of liquid steel can still enhance heat transfer from the molten mixture to the duct.

The distribution of the fuel crust over the outside surface of the duct when the wall failed in 2D and 3D simulations is depicted in Fig. 16. In the 2D case, an appreciable volume of the liquid fuel moved close to the outer surface of the duct and formed the fuel crust from lower-middle to upper locations. However, in the 3D simulation, before the disruption of fuel pins, especially the inner fuel pins, the steel cladding was molten prior to the fuel pellets for its much lower melting temperature and moved near the lower wall as Fig. 5 shows. The inner fuel pins then were disrupted into a number of solid lumps. Interacting with the molten mixture accumulated at the region of disrupted middle and outer pins, the solid lumps occupied most of the near-duct space and limited the convection of liquid steel. As a result, the liquid fuel which appeared later in the pool gathered at a higher position and formed crust via contacting with the low-temperature duct wall near the pool surface as seen from Fig. 5 and Fig. 15(b). According to the analyses on the material distribution in Section 4.3, the formation of the fuel crust may limit the heat flow from the molten pool to the duct. In 2D simulation, although the fuel crust formed on the duct surface above 50 mm axial height, the inner-duct heat flux and the temperature increase of the duct wall were not affected with much more liquid fuel making contact with the outer surface of the duct. As a consequence, in contrast with the 2D simulation in which the sodium had an anomalously high temperature at axial locations close to the surface of the molten pool, the 3D simulation results of the sodium temperature distribution are in good agreement with the test results.

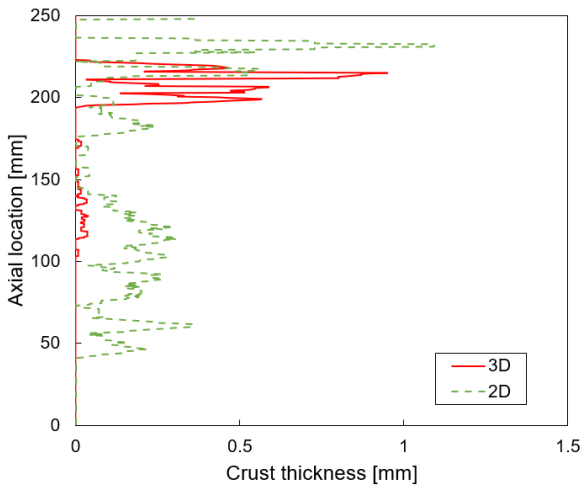

Fig. 16. Axial distributions of the fuel crust in 3D and 2D simulations at failure of the duct wall.

6. Conclusion

This study conducted a 3D simulation using the FVP method coupled with the PMS model to analyze the thermal-hydraulic behaviors during the EAGLE in-pile ID1 test. The simulation reproduced the behaviors of fuel pins melting and disruption, molten pool formation, and heat transfer in the molten mixture, as well as from the molten mixture to the duct wall and the sodium coolant in the ID1 test. Based on the previous 2D simulation (Zhang et al., 2021), the 3D simulation adopted the PMS model to simulate the interaction between the fuel pins and molten mixture. The results of the 3D simulation demonstrated that the pool-to-duct heat transfer was initiated by the direct contact of liquid steel with the outer surface of the duct and the middle-height wall failure was caused due to nuclear heat released by the solid fuel and heat conduction through the liquid steel. Additionally, at a higher position of the pool, although the duct wall could come into contact with the high-temperature solid or liquid fuel, the heat flow would be limited by the fuel crust. The 2D and 3D simulations indicate that pin disruption is important to duct wall failure and it is essential to simulate pin disruption more accurately. Meanwhile, the present results and findings more accurately reproduce the ID1 test and help to understand the thermal-hydraulic behavior during the failure of the duct wall from the phenomenological

perspective. It offers effective data and reasonable validation for FAIDUS, which has been designed for the SFR to mitigate the severe re-criticality events by discharging molten fuel.

Acknowledgements

The authors would like to acknowledge the financial supports by JSPS KAKENHI Grant Number 21K04944 and annual joint research projects of JAEA and Kyushu University. The authors would like to express their gratitude to the support of computer resources under the category of General Projects by the Research Institute for Information Technology, Kyushu University. Zhang. T would like to thank the China Scholarship Council for a State Scholarship (No. 201906380027). The authors thank Edanz (https://jp.edanz.com/ac) for editing a draft of this manuscript.

References

Fink, J.K., Leibowitz, L., 1995. Thermodynamic and transport properties of sodium liquid and vapor. Argonne National Laboratory, ANL/RE-95/2.

Fink, J.K., 2000. Thermophysical properties of uranium dioxide. *J. Nucl. Mater.* 279: 1-18.

Fukuyama, H., Higashi, H., Yamano, H., 2019. Thermophysical properties of molten stainless steel containing 5 mass % B_4C. *Nucl. Technol.* 205(9):1154-1163.

Kamiyama, K., Konishi, K., Sato, I., Toyooka, J., Matsuba, K., Zuyev, V. A., Pakhnits, A. V., Vityuk, V. A., Vurim, A. D., Gaidaichuk, V. A., Kolodeshnikov, A. A., Vassiliev, Y. S., 2014. Experimental studies on the upward fuel discharge for elimination of severe recriticality during core-disruptive accidents in solidum-cooled fast reactors. *J. Nucl. Sci. Technol.* 51(9): 1114-1124.

Kamiyama, K., Konishi, K., Sato, I., Toyooka, J., Matsuba, K., Suzuki, T., Tobita, Y., 2014. An experimental study on heat transfer from a mixture of solid-fuel and liquid-steel during core disruptive accidents in sodium-cooled fast reactor. In: Proc. *of 10th International Topical Meeting on Nuclear Thermal-Hydraulics, Operation and Safety (NUTHOS10)*, Okinawa, Japan, December 14-18, 2014.

Kokubo, H., Nishi, T., Ohta, H., Yamano, H., 2018. Viscosity measurement of nickel and stainless steel aiming at systematic viscosity measurement for molten mixture of stainless steel and boron-carbide. *J. Japan Inst. Met. Mater.* 82(10): 400-402.

Kondo, M., Koshizuka, S., Takimoto, M., 2007. Surface tension model using inter-particle potential force in moving particle semi-implicit method. In: *Proc. of ASME/JSME 2007 5th Joint Fluids Engineering Conference*, San Diego, California, USA, July 30-August 2, 2007.

Konishi, K., Kubo, S., Sato, I., Koyama, K., Toyooka, J., Kamiyama, K., Kotake, S., Vurim, A.D., Gaidaichuk, V.A., Pakhnits, A.V., Vassiliew, Y.S., 2006. The EAGLE project to eliminate the recriticality issue of fast reactors -progress and results of in-pile tests-. In: *Proc. of 5th Korea-Japan Symposium on Nuclear Thermal Hydraulics and Safety (NTHAS5)*, Jeju, Korea, November 26-29, 2006.

Konishi, K., Toyooka, J., Kamiyama, K., Sto, I., Kubo, S., Kotake, S., Koyama, K., Vurim, A.D., Gaidaichuk, V.A., Pakhnits, A.V., Vassiliev, Y.S., 2007. The result of a wall failure in-pile experiment under the EAGLE project. *Nucl. Eng. Des.* 237(22): 2165-2174.

Koshizuka, S., Nobe, A., and Oka, Y., 1998. Numerical analysis of breaking waves using the moving particle semi-implicit method. *J. Numer. Methods Fluid* 26: 751-769.

Liu, X., Ogawa, R., Kato, M., Morita, K., Zhang, S., 2018. Accuracy and stability enhancements in the incompressible finite-volume-particle method for multiphase flow simulations. *Comput. Phys. Commun.* 230: 59-69.

Monaghan, J.J., 2005. Smoothed particle hydrodynamics. *Report on Prog. Phys.* 68: 1703-1759.

Suzuki, T., Kamiyama, K., Yamano, H., Kubo, S., Tobita, Y., Nakai, R., Koyama, K., 2014. A scenario of core disruptive accident for Japan sodium-cooled fast reactor to achieve in-vessel retention. *J. Nucl. Sci. Technol.* 51(4): 493-513.

Toyooka, J., Endo, H., Tobita, Y., Ninokata, H., 2013. A study on mechanism of early failure of inner duct wall within fuel subassembly with high heat flux from molten core materials based on analysis of an EAGLE experiment simulating core disruptive accidents in an LMFBR. *Transactions of the Atomic Energy Society of Japan* 12(1): 50-66. (in Japanese)

Toyooka, J., Kamiyama, K., Tobita, Y., Suzuki, T., 2016. Improvements to the SIMMER code model for steel wall failure based on EAGLE-1 test results. In: *Proc. of 10th Japan-Korea Symposium on Nuclear Thermal Hydraulics and Safety (NTHAS10)*, Kyoto, Japan, November 27-30, 2016.

Woodley, R. E., 1974. The viscosity of molten uranium dioxide. *J. Nucl. Mater.* 50(1): 103-106.

Zhang, S., Morita, K., Fukuda, K., Shirakawa, N., 2007. A new algorithm for surface tension model in moving particle methods. *Int. J. Numer. Meth. Fluid* 55: 225-240.

Zhang, S., Guo, L., Morita, K., Fukuda, K., Shirakawa, N., Yamamoto, Y., 2008. In: *Proc. of 6th Japan-Korea Symposium on Nuclear Thermal Hydraulics and Safety (NTHAS6)*, Okinawa, Japan, November 24-27, 2008.

Zhang, T., Funakoshi, K., Liu, X., Liu, W., Morita, K., Kamiyama, K., 2021. Numerical simulation of heat transfer behavior in EAGLE ID1 in-pile test using finite volume particle method. *Ann. Nucl. Energy* 150: 107856.